Proceedings of ASME Turbo Expo 2011
GT2011
June 6-10, 2011, Vancouver, British Columbia, Canada

GT2011-46073

# A NUMERICAL INVESTIGATION OF ROTATING INSTABILITY IN STEAM TURBINE LAST STAGE

**L. Y. Zhang**
Department of Engineering Science
University of Oxford
Oxford, United Kingdom

**L. He**
Department of Engineering Science
University of Oxford
Oxford, United Kingdom

**H. Stüer**
Siemens AD, Energy Sector,
Fossil Power Generation, Steam Turbine Technology
Mülheim a.d. Ruhr, Germany

## ABSTRACT

In the present study, the unsteady flow phenomenon (identified as rotating instability) in the last stage of a low-pressure model steam turbine operated at very low mass flow conditions is studied through numerical investigations. This kind of instability has been observed previously in compressors and is believed to be the cause of high stress levels associated with the corresponding flow-induced blade vibrations. The overall purpose of the study is to enhance the understanding of the rotating instability in steam turbines at off design conditions. A numerical analysis using a validated unsteady nonlinear time-domain CFD solver is adopted. The 3D solution captures the massively separated flow structure in the rotor-exhaust region and the pressure ratio characteristics around the rotor tip of the test model turbine stage, which compare well with those observed in the experiment. A computational study with a multi-passage whole annulus domain on two different 2D blade sections is subsequently carried out. The computational results clearly show that a rotating instability in a turbine blading configuration can be captured by the 2D model. The frequency and spatial modal characteristics are analyzed. The simulations seem to be able to predict a rotating fluid dynamic instability with the similar characteristic features to those of the experiment. In contrast to the previous observations and conventional wisdom, the present work reveals that the formation and movement of the disturbance can occur without 3D and tip-leakage flows, even though a quantitative comparison with the experimental data can only be expected to be possible with full 3D unsteady solutions.

## INTRODUCTION

To reduce power generation costs and meet environmental requirements, combined cycle power plants have been widely developed. High efficiency is required in such power plants without sacrificing long term reliability and flexibility. It brings challenges to steam turbine designs because these turbines will no longer function individually but use the steam produced by the heat from the exhaust of a gas turbine. As a result the steam turbines can face highly variable operation conditions including extreme low mass flow conditions. Such off-design conditions may cause aeroelastic problems to turbine blades, especially in the last stage of a LP turbine where the blades are relatively long and therefore vulnerable to flow induced vibrations. Since a steam turbine may undergo the part-load conditions during operation for a considerable length of time, high dynamic stresses that are associated with the blade excitation must be avoided or at least controlled to be below a certain level specified by the blade fatigue criteria. Therefore it is necessary to investigate the flow behavior of last stage LP turbines and corresponding aeroelastic phenomena under these low mass flow off-design conditions. The knowledge will benefit the design process in identifying and reducing the risks of a mechanical failure. It is also helpful in extending the working range of a steam turbine and improving the operational flexibility.

For turbomachinery blade rows operated at a low mass flow condition, self-excited rotating instabilities are often observed. However, they are mostly for the compressor configurations. There are many studies of rotating instabilities, either in terms of understanding stall inception mechanisms, e.g. [1] or in simulating the process, e.g. [2] [3] [4]. Research efforts are also made in relation to understanding acoustic characteristics of the instabilities in compressors and fans at a stable operational point, e.g. [5] [6] [7]. In the context of compressors, rotating instability is believed to be responsible for certain types of excitation for rotor blade vibrations and the inception of stall and surge [8].

An experimental study on a last stage model turbine at low mass flow conditions was conducted in the University of Stuttgart [9]. During the analysis on the measured unsteady pressure field and the relation between high amplitude disturbance and the excitation of the blades, a rotating instability was indentified for the first time for turbine blade configurations. In the measured pressure signals, sharp unsteady pressure peaks were located at certain frequencies other than blade passing frequency (BPF) or its multiples. A group of small amplitude peaks were also found evenly spaced between the main humps (Figure 1). These are typical features of rotating instability and suggest that some kind of rotating 'periodic' flow structure may be related to the pressure disturbances. Apart from the above piece of work, rotating instability in a turbine configuration has been rarely reported, little is known about the fundamental onset mechanisms, as well as whether or not the rotating instability in turbine is different from or similar to that in a compressor.

In general for compressors, tip clearance flow is believed to be crucial to the rotating instability phenomena because the detected pressure disturbance is prominent in the region near a blade tip. The tip clearance vortex flow is commonly considered to play an important role in forming the rotating instability structure [10], but the flow physics seems to be case-sensitive. Some criterion based on the detail knowledge of the tip flow was proposed for certain compressor stage configurations [11]. The tip clearance ratio was also considered a crucial parameter and was investigated experimentally [12]. In a study with an azimuthal analysis of unsteady pressures measured at the casing wall of a low-speed axial-flow fan [13], rotating instability was compared with rotating stall observed at the same time. The latter is characterized as an 'almost-frozen' flow pattern rotating circumferentially, while the former shows a fluctuating nature. A similar study [14] shows that the pressure peak pattern could be explained as a 'rotating loudspeaker': a source frequency in a rotating frame, which is able to excite pressure waves with various nodal diameters, leading to the frequency peaks as observed in the fixed frame. So far experimental and numerical studies on rotating instabilities have been carried out to explain the pressure patterns measured and to reveal the corresponding flow structure [15]. Yet no CFD work has been reported in open literature in relation to rotating instabilities for turbine blade rows. In addition, although the phenomenon is assumed to be related to the non-synchronous blade vibration, no direct link between the excitation and the instability has been identified exclusively.

The present work is motivated to identify and understand the mechanisms and basic characteristics of a rotating instability in a turbine blading configuration. A computational research is carried out for this in particular in the context of potential turbine blade aeroelastic problems. It should be pointed out that unlike rotating stall in compressors that may lead to a surge and the complete breakdown of the flow pattern, rotating instability in steam turbines can stay in a sustainable manner at a globally stable condition for a long time. Therefore it is important to be able to numerically predict the stress level on the blades and ensure it below the admissible limits set in a design phase. The work is also motivated by the need to improve performance of the turbines at off-design conditions and to extend the working range.

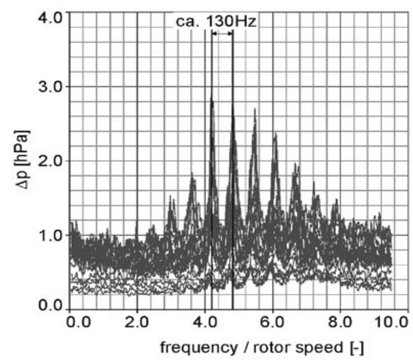


Figure 1 Frequency spectra of total pressure in axial gap of the last stage of a model turbine [9].

## NOMENCLATURE

| | |
|---|---|
| A | The corresponding plane area, $m^2$ |
| BPF | Blade passing Frequency |
| Cax | Blade chord length in axial direction, m |
| $e$ | Internal energy, J/kg |
| $h$ | Enthalpy |
| $P_o$ | Total pressure, Pa |
| $P_s$ | Static pressure, Pa |
| $PS$ | Pressure surface |
| r | Radius, m |
| RANS | Reynolds-averaged Navier-Stokes equations |
| RF | Rotor Rotational Frequency |
| RIF | Rotational Instability Frequency |
| $SS$ | Suction surface |
| $u$ | Axial velocity, m/s |
| $\dot{V}$ | Volume flow, $m^3/s$ |
| $v$ | Tangential velocity, m/s |
| $w$ | Radial velocity, m/s |
| $\mu$ | Dynamic viscosity, Pas |
| $\omega$ | Angular frequency, 1/s |
| $\varphi_r$ | Relative volume flow rate, $\varphi = \frac{\dot{V}}{A\omega r}$, $\varphi_r = \frac{\varphi}{\varphi_{design}}$ |
| $\rho$ | Density, $kg/m^3$ |
| $\Omega$ | Angular velocity, rad/s |

## NUMERICAL MODELLING

The governing equations here are the three dimensional Reynolds averaged Navier-Stokes equations in cylindrical coordinates $(x,\theta,r)$ in an absolute frame of reference.

$$\frac{\partial}{\partial t}\iiint \boldsymbol{U} dV + \oiint [\boldsymbol{F}\cdot n_x + \boldsymbol{G}\cdot n_\theta + \boldsymbol{H}\cdot n_r] dA \\ = \iiint \boldsymbol{S}_i dV + \oiint [\boldsymbol{F}_v\cdot n_x + \boldsymbol{G}_v\cdot n_\theta + \boldsymbol{H}_v\cdot n_r] dA \tag{1}$$

where,

$$\boldsymbol{U}=\begin{bmatrix}\rho\\ \rho u\\ \rho vr\\ \rho w\\ \rho e\end{bmatrix},\quad \boldsymbol{F}=\begin{bmatrix}\rho u-\rho u_g\\ \rho uu+P-\rho uu_g\\ (\rho uv-\rho vu_g)r\\ \rho uw-\rho wu_g\\ \rho uh-\rho eu_g\end{bmatrix},\quad \boldsymbol{G}=\begin{bmatrix}\rho v-\rho v_g\\ \rho uv-\rho uv_g\\ (\rho vv+P-\rho vv_g)r\\ \rho vw-\rho wv_g\\ \rho vh-\rho ev_g\end{bmatrix},$$

$$\boldsymbol{H}=\begin{bmatrix}\rho w-\rho w_g\\ \rho wu-\rho uw_g\\ (\rho wv-\rho vw_g)r\\ \rho ww+P-\rho ww_g\\ \rho wh-\rho ew_g\end{bmatrix},\quad \boldsymbol{S}_i=\begin{bmatrix}0\\ 0\\ 0\\ \rho v^2/r\\ 0\end{bmatrix}$$

$\boldsymbol{S}_i$ is the inviscid source term that accounts for the rotating effects.

$$\boldsymbol{F}_v=\begin{bmatrix}0\\ \tau_{xx}\\ \tau_{x\theta}r\\ \tau_{xr}\\ -q_x+u\tau_{xx}+v\tau_{x\theta}+w\tau_{xr}\end{bmatrix},\boldsymbol{G}_v=\begin{bmatrix}0\\ \tau_{\theta x}\\ \tau_{\theta\theta}r\\ \tau_{\theta r}\\ -q_\theta+u\tau_{\theta x}+v\tau_{\theta\theta}+w\tau_{\theta r}\end{bmatrix},$$

$$\boldsymbol{H}_v=\begin{bmatrix}0\\ \tau_{rx}\\ \tau_{r\theta}r\\ \tau_{rr}\\ -q_r+u\tau_{rx}+v\tau_{r\theta}+w\tau_{rr}\end{bmatrix}$$

$$\tau_{xx}=2\mu\frac{\partial u}{\partial x},\tau_{\theta\theta}=2\mu\left(\frac{1}{r}\frac{\partial v}{\partial\theta}+\frac{w}{r}\right),\tau_{rr}=2\mu\frac{\partial w}{\partial r}$$

$$\tau_{r\theta}=\tau_{\theta r}=\mu\left(\frac{1}{r}\frac{\partial w}{\partial\theta}-\frac{v}{r}+\frac{\partial v}{\partial r}\right)$$

$$\tau_{xr}=\tau_{rx}=\mu\left(\frac{\partial u}{\partial r}+\frac{\partial w}{\partial x}\right),\tau_{x\theta}=\tau_{\theta x}=\mu\left(\frac{\partial u}{r\partial\theta}+\frac{\partial v}{\partial x}\right)$$

$(u_g, v_g, w_g)$ are moving grid velocities. If the mesh is rotating in an angle velocity of $\Omega$, as the case often seen in the rotor row of turbomachinary, then the moving grid velocity is $(0,\Omega r,0)$.

The Spalart-Allmaras one-equation turbulence transport model is adopted here [16]. For the solid wall surface, the slip wall condition is applied with the shear stresses being evaluated from the log law so that a coarser mesh can be used to reduce computing time. For inlet and exit boundaries, the boundary condition for the steady flow solutions (specifying inlet stagnation pressure, stagnation temperature, inlet flow angle, and exit static pressure) is adopted. At the circumferential boundaries of a multi-blade passage domain a direct periodic boundary condition is implemented.

The spatial discretization for the equations is the second-order cell-centered finite volume scheme. The fluxes are calculated from the flow variables at the cell surface. The summation is taken along the boundary surfaces. Second and fourth-order adaptive smoothing is used to suppress numerical oscillations [17]. The time-marching solution is performed by four-stage Runge–Kutta integration, accelerated by a time-consistent or connectivity based multi-grid techniques [18]. In a multi-blade row calculation meshes are fixed to the stator or rotor blades and patched at the interface. Local instantaneous information is transferred directly across the interface by a second-order interpolation and correction method [18].

## STEADY FLOW VALIDATION CASE

In the current study the time-domain nonlinear time marching solver is used for a steady flow first as a baseline solution. A low-speed 2D LP turbine blade sections in a linear cascade with large scale flow separation on the pressure side is calculated as a test case. The surface pressures for this case were measured in the corresponding experiment [19]. In the calculations, the blade is scaled up by a factor of 2.3. The computational mesh for this cascade is O-mesh with the total mesh points of 46,338 for 5 blocks in a single-passage domain.

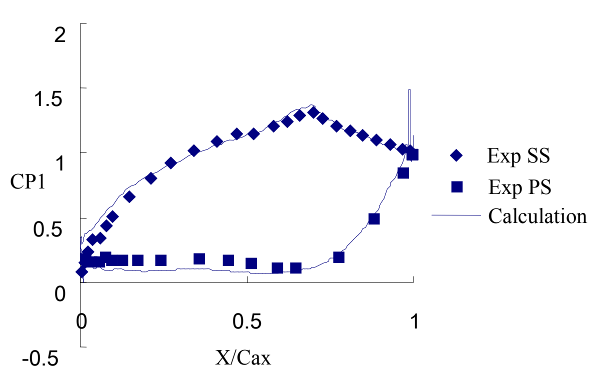


Figure 2 Steady pressures compared with experiment [19]. (inlet flow angle 20°, Reynolds number 220,000)

Figure 2 shows the steady pressure distributions along the blade surface compared with the experimental data, for the inlet flow angle of 20 deg. The comparison with the experiment shows good agreement. From the computational result of stagnation pressure/entropy loss (Figure 3) the pressure surface large scale separation can be clearly observed. The boundary layer on the pressure side separates from the leading edge and reattaches at a position over half the axial chord. The calculation captures the separation flow and surface pressure very well for this case. The flow physics is similar to the case of last-stage rotor blades at low mass flow rate conditions, where the high back pressure will lead to a reduced axial flow velocity and a high negative incidence angle to the rotor and lead to a massive separation on the pressure surface.

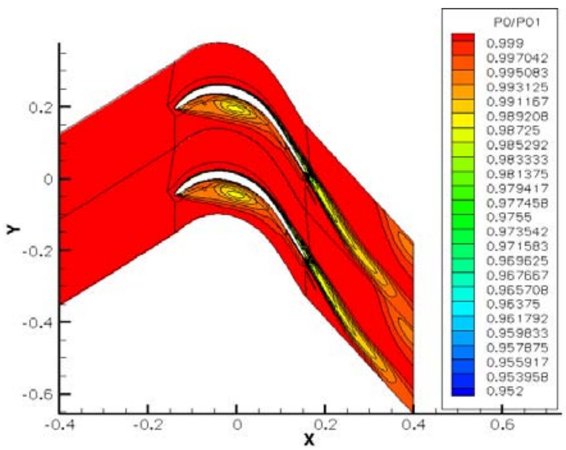


Figure 3 Contours of steady total pressure loss.

## MODEL TURBINE STAGE WITH SEPARATION IN DIFFUSOR

The model turbine stage tested in the University of Stuttgart [9] [20] which exhibits the rotating instabilities is investigated here. Both the blading profiles of stator and rotor are three dimensional. To reduce the computational cost we make an approximation of the blade count ratio to 2:3, which means 2 stators and 3 rotors passages in the computational domain. The rotor row rotates at a frequency of 210 Hz. A 3D calculation at the design condition is conducted first as a baseline. The results are compared with those from a well-established 3D time-marching RANS code [21] using the mixing plane method for multistage simulations, showing a good overall agreement in the basic stage aerothermal performance parameters between the two codes.

To further simulate the condition in the experiment [20], calculations on the last stage of the model turbine are carried out with a diffuser attached, as shown in Figure 4. The flow pattern in the 3D stage configuration is quite different from the scenario in 2D cascades. The flow separation takes place in the diffuser behind the rotor row in the experiment (Figure 6). To form this separation and change the flow condition through the stage, the exit of the diffuser is partially blocked. A two rows multi-passage H-mesh domain is adopted. 37 x 93 x 46 mesh points are used for each stator passage, 37 x 111 x 46 mesh points are used for each rotor passage and 37 x 100 x 46 x 3 mesh points in total are used for the diffusor. A direct periodic boundary condition is adopted at circumferential boundaries of the multi-passage domain. Tip clearance is not included in the current study.

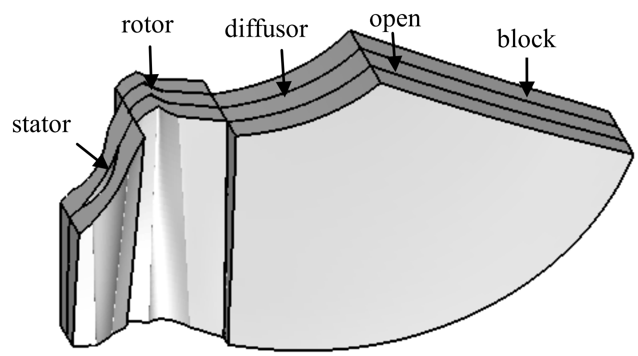


Figure 4 Computational domain of the model turbine stage.
(2 stator passages, 3 rotor passages)

In the experiment, the measured flow field in front of and behind the rotor blade indicates strong unsteadiness close to the outer flow boundary between 11% and 22% of the design volumetric flow [20]. Thus several operation conditions of low volume flow rate are considered in the calculation to provide a baseline of the flow characteristics to compare with the experiment (Figure 7).

Figure 5 shows the calculated streamlines in the turbine stage. The flow pattern at the off-design condition (Fig.5b) is dramatically changed from the case at the nominal condition (Fig.5a), especially at the diffusor part. The separation structure behind the rotor is well captured by the calculation (comparing Figure 5b and Figure 6. A big vortical structure with the massive flow separation is formed near the hub. In the experiment the reverse flow goes from the exit of the diffuser to the exit of the rotor row and affects the flow angle in the rotor row (Figure 6). This feature is also clearly revealed by the calculation (Fig.5b).

The calculated static pressure ratio at the tip region of the rotor blade row is compared with the measurement results at various operating conditions in Figure 7. The calculation shows a good agreement with the measurement at off-design low flow conditions. At the relative volume flow rate less than 26% of the design condition, the ratio between the exit static pressure and the inlet static pressure of the rotor tip goes higher than 1, which means the tip region of the turbine rotor blade now functions as a compressor. Meanwhile the overall turbine stage can still keep working persistently in a stable manner without a global reverse flow which would otherwise result in a complete breakdown of stage performance as in a compressor surge.

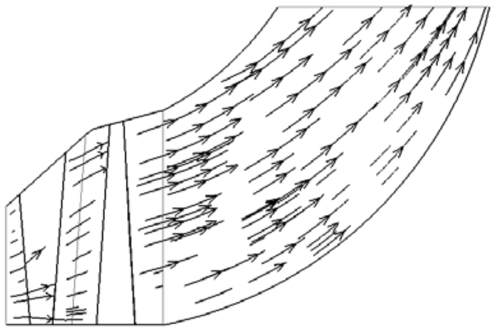

a) Nominal condition

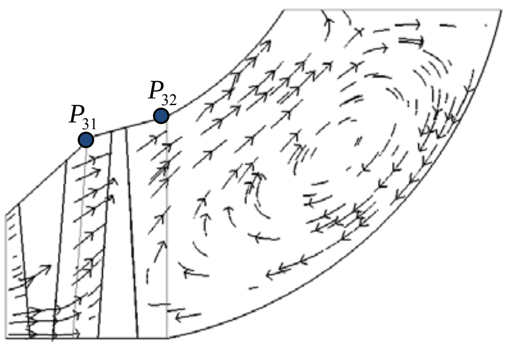


b) $\varphi_r = 0.258$

Figure 5 Calculated streamlines in the model turbine stage.

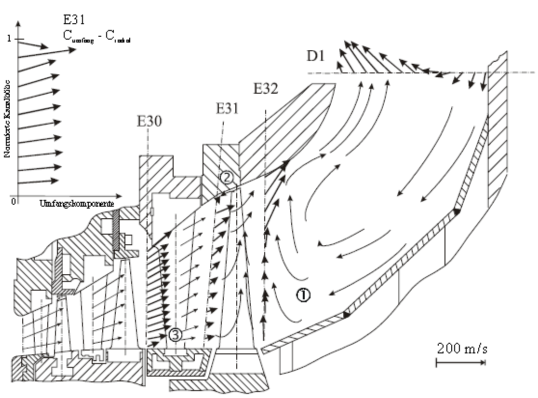


Figure 6 Experimental flow pattern ( $\varphi_r = 0.22$ ) [20].

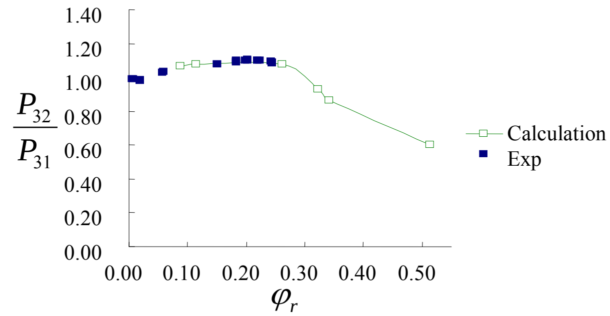


Figure 7 Calculated rotor tip pressure ratio compared with the measurement [20]. ( $P_{31}$ and $P_{32}$ are taken from the locations shown in Figure 5b)

Although the off-design conditions are simulated and the massive separation is captured in the 3D calculations, no rotating instability is observed from the 3D results so far. It is suspected to be due to the rather limited computational domain size in the circumferential direction. The wavelength of the circumferential non-uniformity is restricted by the periodic boundary condition. For the 3D simulations, the computational domain only contains 2 stator passages and 3 rotor passages, which are not considered to be large enough. Further 3D studies are on-going.

## ROTATING INSTABILITY IN 2D CONFIGURATION

As 3D whole annulus unsteady calculations are highly time-consuming, a first attempt is made on 2D whole annulus multi-passage calculations. The aim is to help to gain some fundamental understanding on the onset mechanism of rotating instabilities in turbines. Although 3D flow effects such as those due to tip leakage are often regarded as essential elements for the onset of a rotating instability in compressors, it is of interest to examine what might and can happen in a pure 2D configuration. For this reason 2D calculations should provide a reference case before considering the tip clearance flow and other 3D effects.

Blade profiles from the near hub (10% span) and near tip (90% span) 2D sections are simulated respectively (Figure 8). A uniform condition is set at the inlet. Both the nominal flow condition and off-design low-flow conditions are obtained by changing the outlet static pressure. The extreme low mass flow conditions are achieved with a large increase in the exit static pressure.

 

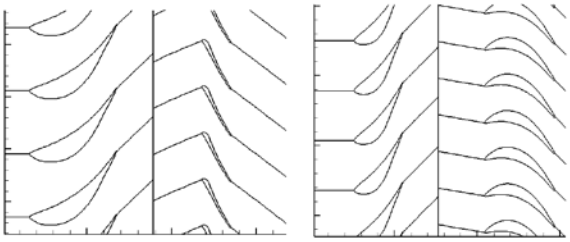

a) 90% span b) 10% span

Figure 8 2D Multi-passage configurations.

Figure 9 shows the pressure contours of the near tip plane at the nominal flow condition. Flow throughout the stage reveals a clear passage-passage periodicity, subject only to the expected rotor-stator blade row interactions. No non-synchronized unsteadiness is detected at the nominal condition.

For a low mass flow condition, a large blockage that originates from the separation and shedding of vortical flow structures in rotor passages is shown. A clear circumferential non-uniformity starts to appear, as shown in Figure 10. These disturbance structures rotate and evolve across the annulus and result in large amplitude pressure fluctuations throughout the stage.

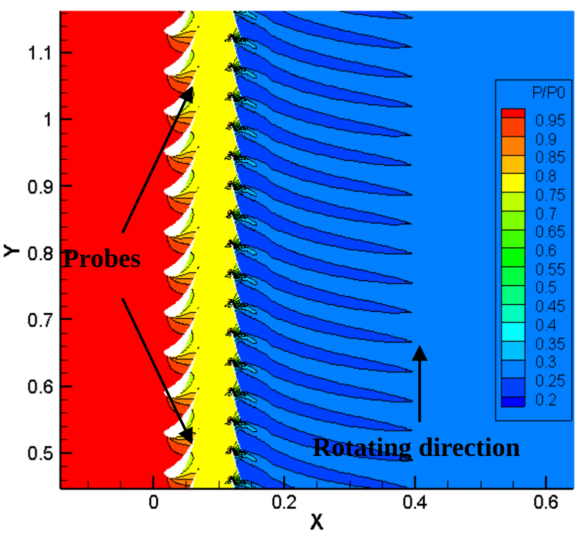


Figure 9 Pressure contour on 90% span section. (Nominal flow condition, 100%)

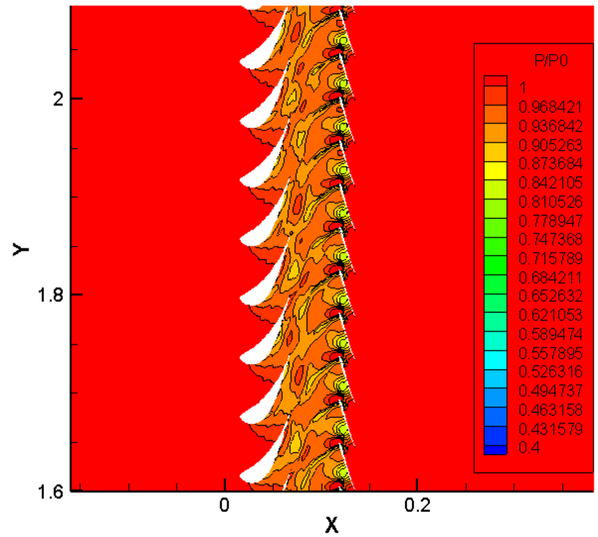


Figure 10 Pressure contours on 90% span section. (Relative flow rate: 65.6%)

Several numerical probes are placed in the stator middle passage positions right behind the blades (Figure 9). The time traces of the unsteady pressures at these probe points are recorded. Fourier analysis (Figures 11, 12, 14) of the unsteady pressure signals from the probes show different frequency patterns for different relative mass flow rates. At a relatively high mass flow rate (74.8% of the nominal), no instability is triggered. The disturbances which can be observed from the frequency spectrum are only those of blade passing frequency (BPF), rotor rotating frequency (RF) and its multiples (Figure 11).

| Relative mass flow rate | Dominant frequency (Hz) |
|---|---|
| 74.8% | NA |
| 65.6% | 1649 |
| 64.0% | 2215 |

Table 1 Rotating instability frequency versus relative flow rate.

If the relative mass flow rate is further decreased to 65.6%, a distinctively different spectrum arises (Figure 12). A group of peaks are found with a dominant frequency at about 1649 Hz, which is not synchronous with either BPF or RF. It is recognized that this frequency is considerably higher than the rotating instability frequency (RIF) in the experiment [9], which is about 1000 Hz. It has to be pointed out that the flow rate here is normalized by the local 2D reference value, which may well be different from the condition in the 3D configuration. So the results are not directly comparable to the experimental data. The finding is nevertheless interesting. The broadband hump is superimposed with evenly spaced peaks, which is similar to the rotating instability frequency pattern in the experiment (Figure 1). The largely constant interval between particular peaks is about 172 Hz, as shown in Figure 12b (in the experiment it is about 130 Hz). Tonal components at difference cross-coupled sub-harmonic frequencies such as (BPF±RIF) are also visible. The blade passing disturbances shown by BPF is not prominent now compared with the magnitude of the rotating instability unsteadiness (RIF).

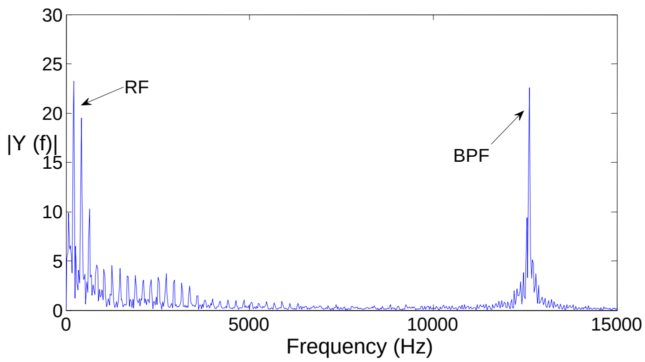


Figure 11 Frequency spectra (90% span section) of unsteady pressures (relative mass flow rate: 74.8%).

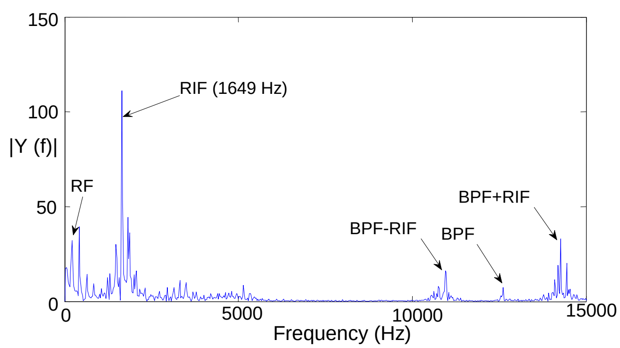


a) Overall Spectrum (0-15000 Hz).

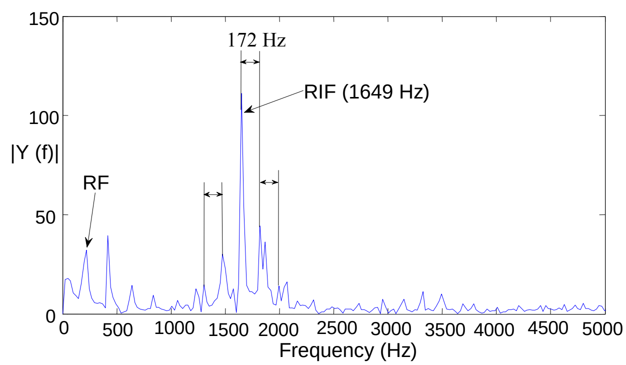


b) Close up (0-5000 Hz).

Figure 12: Frequency spectra (90% span section) of unsteady pressures (relative mass flow rate: 65.6%).

Figure 13 shows the time traces of the unsteady pressure signals taken in three stator passages. The pressure amplitudes of passage 10 and 20 are shifted by -4000 Pa and -2000 Pa respectively for clarity of presentation. It shows the pressure field is under fluctuation with amplitudes over 1000 Pa. However the disturbances stay within a stable range (i.e. in a limit cycle pattern) that will not lead to a global flow breakdown as in a surge for a compressor system. There are phase differences between the time traces of the three passages. Passage 10 is leading passage 20 and passage 30. This means that relative to the stator, the flow pattern moves in the same direction as the rotation of the rotor.

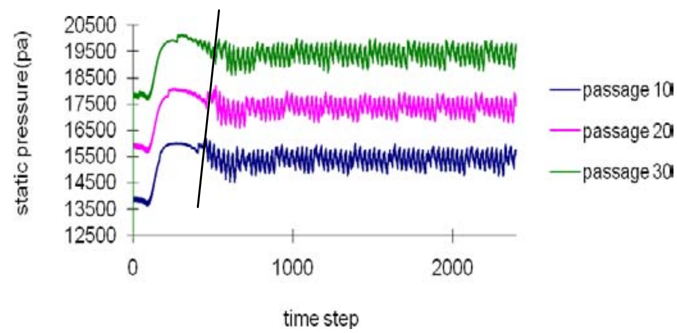


Figure 13 Time trace of static pressure of 90% span section. (Relative mass flow rate: 65.6%, amplitudes of passage 10 and 20 are shifted by -4000 Pa and -2000 Pa respectively.)

When the mass flow rate is further decreased with a higher back pressure to 64 % of the nominal flow rate, the signal of the instability (RIF) is much stronger than the unsteadiness of the blade passing one (BPF) (Figure 14). Also the dominant frequency shifts to a higher frequency (about 2215 Hz) now (Table 1).

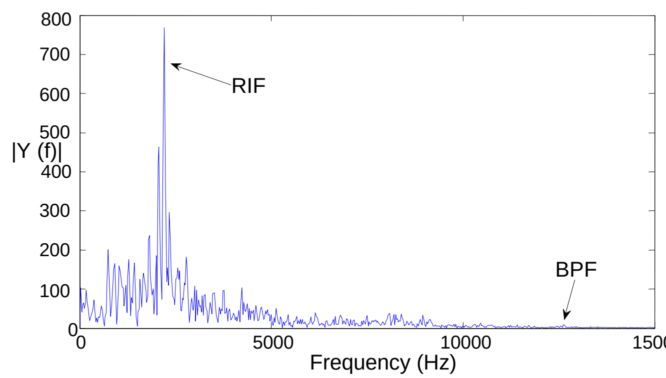


Figure 14 Frequency spectra (90% span section) of unsteady pressures (relative mass flow rate: 64.0%).

An attempt is also made to identify the circumferential nodal pattern of the disturbances (i.e. the number of rotating instability events or cells). A circumferential spatial Fourier analysis is carried out at several different time instants for the relative mass flow rate of 65.6%. The spectrum shows a dominant spatial nodal number of 16 (Figure 15). The fundamental nodal diameter number 1 is also visible. This suggests that there are about 16 major instability flow structures across the whole annulus moving at a certain speed. According to the phase angles of signals from three adjacent passages in the stator row (Table 2), a phase lag can be observed for passages upward (Figure 10) at the dominant frequency of 1649 Hz. This phase relation is consistent with that revealed with the time traces (Figure 13).

All the above results seem to support that these fluctuating structures are rotating in the same direction as the rotor as seen in the stator frame of reference. And the rotating frequency of the group of these 16 disturbances is about 100 Hz, which is about half the rotor speed. So in the rotor frame of reference, the instability sources are moving at a half of the rotation speed but in the opposite direction to that of the rotation. It is worth noting that the overall characteristics are quite similar to some previous observations for compressors, e.g. [15].

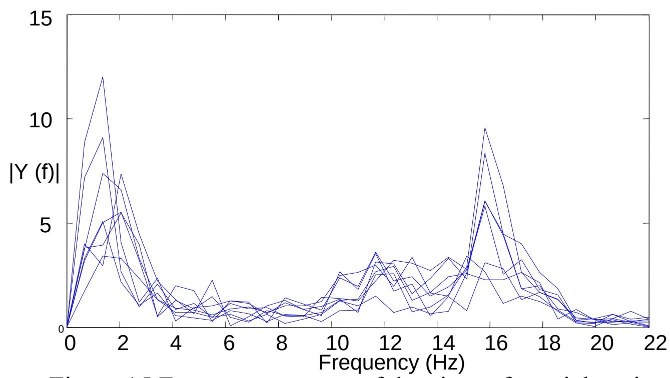


Figure 15 Frequency spectra of the circumferential static pressure of 90% span at different time instances.

| passage | Phase angle |
|---|---|
| 10 | -0.07568 |
| 11 | -1.62106 |
| 12 | -2.19973 |

Table 2 Phase angle (frequency 1649 Hz).

Although these 2D calculations are of a qualitative nature, a relevant question can be asked regarding the mesh dependence: to what extent may these calculated rotating instabilities be dependent on the mesh density? It is important that the observed rotating instability behavior is qualitatively independent of mesh density for the range of the values used here. Two meshes (Figure 16) are adopted to examine the mesh dependency of the calculations for the blade tip section (Figure 8, left) with a smaller circumferential domain size. The details of the meshes are in Table 3. The domain containing 4 stator passages and 6 rotor passages is adopted here. The original mesh has the same mesh density per passage as in the full annulus calculations shown in Figures 9, 10.

| | original | | Refined | |
|---|---|---|---|---|
| Number of grids | stator | rotor | stator | rotor |
| Streamwise | 121 | 136 | 181 | 204 |
| Pitchwise | 37 | 37 | 55 | 55 |
| In total (per passage) | 4477 | 5032 | 9955 | 11220 |

Table 3 Mesh Densities for 2D configurations (90% span).

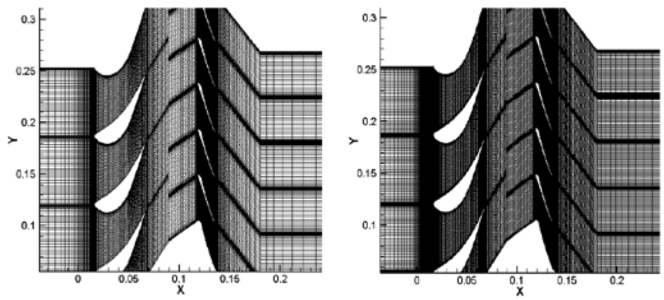

Figure 16 Computational meshes (90% span section). (Left: original; right: refined)

The rotating instability is also identified in the smaller domain calculations at a relative mass flow rate of 70.4%, although the circumferential wave length is changed from the whole annulus case. The frequency spectra from the original mesh and the refined mesh capture the same main frequency peaks for the RIF, BPF and the cross-coupled sub-harmonic frequencies (Figure 17). This mesh dependency study shows that the original mesh density adopted is sufficient to capture consistently the main characteristics of the rotating instability.

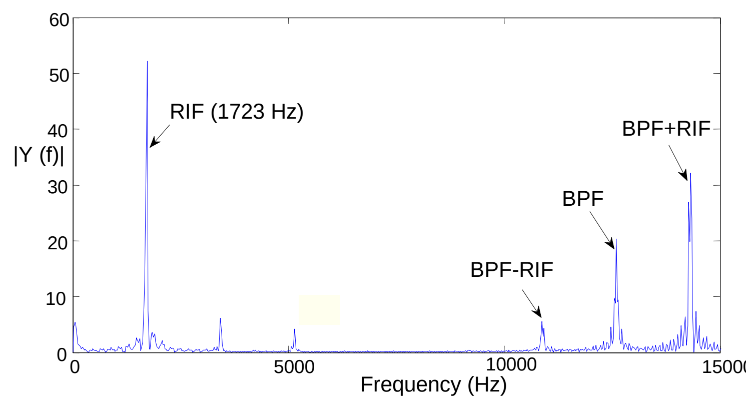


a) Original mesh

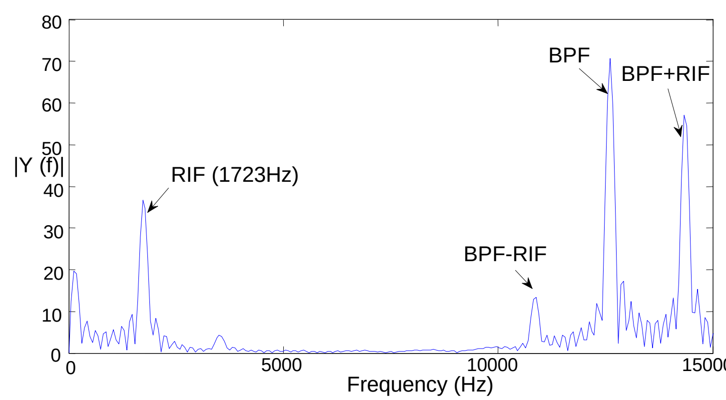


b) Refined mesh

Figure 17 Frequency spectra (90% span section) of unsteady pressures from the two meshes (relative mass flow rate: 70.4%).

Now we turn the attention to the near hub section (10% span). The results for the near hub section are quite different from those for the near tip section. The hub section seems much more resistant to a rotating instability development at a low mass flow rate. Even when the mass flow rate is decreased to 14.71% of the nominal, no noticeable rotating instability is detected. The time traces of static pressures in three stator passages (with a shift of -4000 Pa and -2000 Pa at passage 10 and 20) are shown in Figure 18. In a clear contrast to the counterpart for the tip (Figure 13), the hub results show no clearly identifiable fluctuations. The only peaks visible in the corresponding frequency spectra are at BPF and frequencies near zero which is due to the very slow changes in pressures (Figure 19). With the rotor blade profile near the hub having a high camber (Figure 8b), it tends to have a larger separation on the pressure side with a high blockage, leading to the lower mass flow rate compared with the tip blade section (compare Figure 20 to Figure 10). However the high camber blading also seems to localize the effects of the separation bubble and reduce the likelihood of forming a circumferential synchronized disturbance. Thus a circumferentially travelling flow pattern seems to be more difficult to develop across the annulus near the hub.

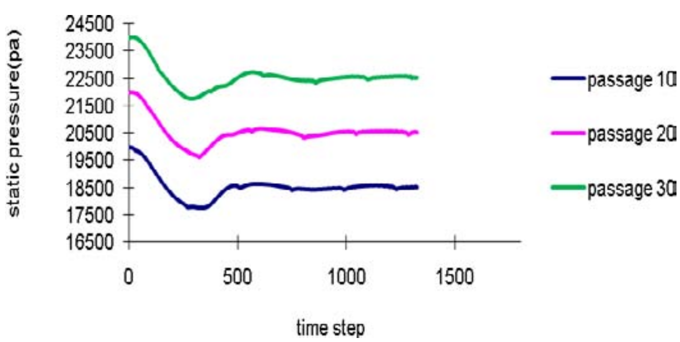

Figure 18 Time traces of static pressures of 10% span section. (Relative mass flow rate: 14.71%. The amplitudes of passage 10 and 20 are shifted by -4000 Pa and -2000 Pa respectively.)

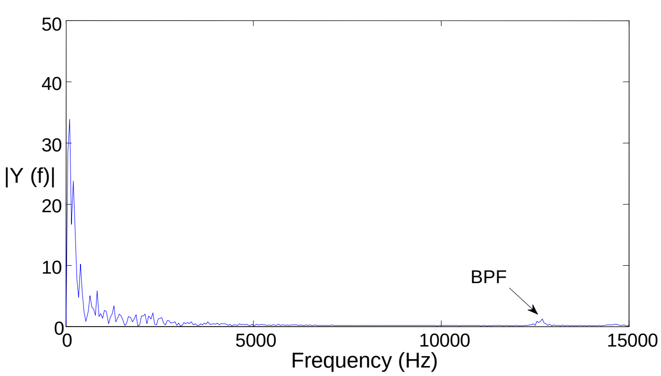

Figure 19 Frequency spectra (10% span section) of unsteady pressures (relative mass flow rate: 14.71%).

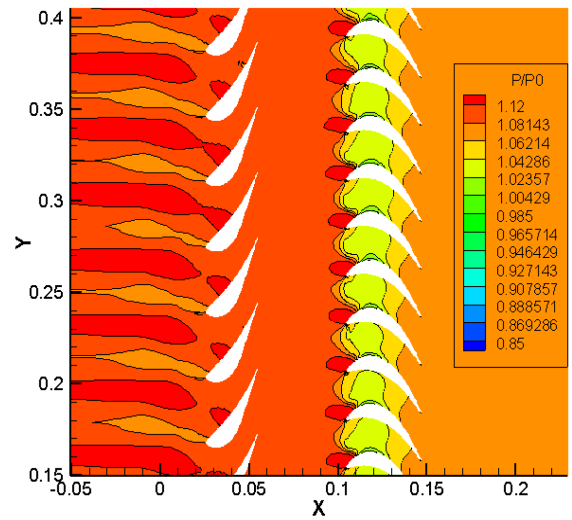

Figure 20 Pressure contours on 10% span section. (Relative flow rate: 14.71%)

The rotating instability observed in 2D configurations shows some similarities to the experiment [9]. Although 3D vortical structures associated with a tip clearance flow may be linked to a rotating instability as commonly suggested, the present analysis seems to indicate that they may not necessarily be the cause of the instability. The present results show that under a low mass flow condition, a similar rotating pattern can be produced in a purely 2D blading configuration. The distinctively different characteristics of the tip and hub sections imply that the blading geometry makes a difference in the onset, formation and development of the rotating instability for turbine blades.

## CONCLUDING REMARKS

Numerical studies have been conducted to understand the rotating instability previously experimentally identified at low mass flow rates in a model steam turbine stage. An initial CFD analysis using a time-domain RANS solver is able to capture a large scale separated flow pattern, which is compared well with the experimentally observed one. The 3D vortical flow pattern observed in the experiment is reproduced in the 3D calculation.

To identify the rotating instability phenomenon through calculations, further analyses with two distinctively different 2D blade profiles from the model turbine blades are carried out with whole annulus simulations at both the nominal and a range of low flow off-design conditions. A number of circumferentially evenly positioned numerical probes are located in the stationary frame to detect rotating disturbances. The results consistently show that a rotating pattern non-synchronized with the rotor speed exists at low mass flow conditions. The dominant frequency for the tip section identified by the Fourier transform is a higher (by 50%) than the experimental value and shifts when the mass flow rate is changed. The circumferential wave number and the rotating speed are also analyzed. The results suggest that the rotating speed of the patterns as seen in the stationary frame of reference is about a half of the rotor rotation speed. On the other hand, the near hub section is much more stable with no clearly identifiable rotating patterns found at low mass flow conditions. These 2D simulations results can be used as a reference to understand truly 3D effects on the onset and development of rotating instabilities in steam turbines.

## ACKNOWLEDGEMENT

The authors wish to acknowledge Siemens Energy for the financial support and for the permission to publish this work.

## REFERENCES

1. Day I.J., “Stall inception in axial flow compressors”, ASME Journal of Turbomachinery, Vol. 115, 1993.

2. He L., “Computational study of rotating stall inception in axial compressors, AIAA Journal of Propulsion and Power, 13,(1), 1997

3. Hah, C., Schulze, R., Wagner, S., and Hennecke, D. K., ‘‘Numerical and Experimental Study for the Short Wavelength Stall Inception in a Low-Speed Axial Compressor,’’ Proc. Fourteenth ISABE Conference, IS-234,1999

4. He L. and Ismael J. O., “Computations of bladerow stall inception in transonic flows”, The Aeronautical Journal, Vol.103, No.1025, July 1999.

5. Bent P. H., McLaughlin D. K., and Thompson D. E., “The influence of discharge configuration on the generation of broadband noise in centrifugal turbomachinery”, D. DGLR/AIAA 92-02-099, 1992

6. Mongeau, L., and Quinlan, “An Experimental Study of Broadband Noise Sources in Small Axial Fans”, International Symposium on Fan Noise INCE, Senlis, France, Sept. 1–3, 1992

7. Mongeau L., Thompson D. E., McLaughlin D. K., “Sound generation by rotating stall in centrifugal turbomachines”, Journal of Sound and Vibration, 163(1),1-30, 1993

8. Cumpsty N.A. , “Compressor Aerodynamic”, 2nd Edition, Krieger Publishing Company, April 2004

9. Gerschütz W, Casey M, and Truckenmüller F, “Experimental investigations of rotating flow instabilities in the last stage of a low-pressure model steam turbine during windage”, Proc. IMechE Vol. 219 Part A: J. Power and Energy, 2005

10. Hah C., Voges M., Mueller M. and Schiffer H. P., “Characteristics of Tip Clearance Flow Instability in a Transonic Compressor”, Proceedings of ASME Turbo Expo 2010: Power for Land, Sea and Air GT2010 June 14-18, Glasgow, UK, 2010

11. Vo H. D., “Role of Tip Clearance Flow in Rotating Instabilities and Nonsynchronous Vibrations”, Journal of Propulsion and Power Vol. 26, No. 3, May–June 2010

12. Kameier F., Neise W., “Rotating Blade Flow Instability as a Source of Noise in Axial Turbomachines”, Journal of Sound and Vibration, 203(5), 833-853,1997

13. Liu J. M., Holste F., Neise W., “On the azimuthal mode structure of rotating blade flow instabilities in axial turbomachines”, AIAA Meeting Papers on Disc, A9630853, AIAA Paper 96-1741, May 1996

14. Baumgartner M., Kameier F., Hourmouziadis J., “Non-Engine Order Blade Vibration in a High Pressure Compressor”, ISABE-Twelfth International Symposium on Airbreathing Engines, Melbourne, Australia, September 10-15, 1995

15. März J., Hah C., Neise W., “An Experimental and Numerical Investigation into the Mechanisms of Rotating Instability”, Journal of Turbomachinery, Vol. 124/367-375, July 2002

16. Sparlart P. R., and Allmaras S. R., “A One-Equation Turbulence Model for Aerodynamic Flows”, AIAA Paper 92-0439, Jan. 1992

17. Jameson A., Schmidt W., and Turkel E., “Numerical Solutions of the Euler Equation by Finite Volume Method Using Runge–Kutta Time-Stepping Scheme”, AIAA Paper 81-1259, June 1981

18. He L., “3-D Navier-Stokes Analysis of Rotor-Stator Interactions in Axial-flow Turbines”, Proc. IMech. E, Part A, 214, pp 13–22, January, 2000

19. He L., “Unsteady Flow in Oscillating Turbine Cascades”, Journal of Turbomachinery, Vol. 120, APRIL 1998

20. Truckenmüller F., “Untersuchungen zur aerodynamisch induzierten Schwingungsanregung von Niederdruck-Laufschaufeln bei extremer Teillastt“, PhD Dissertation, the University of Stuttgart, 2002

21. Denton, J.D. The calculation of three-dimensional viscous flow through multistage turbomachine, ASME Journal of Turbomachinery, Vol. 114, No. 1, 1992.